Study of the direction of motion over an Eight pattern trajectory for a traction kite Full downwind

Julien Bernard-Lameau, Jérémy Loustau-Laguide, Kostia Roncin, Benjamin Chouvion, Loïc Daridon

19e Journées de l'Hydrodynamique
26 – 28 novembre 2024, Nantes

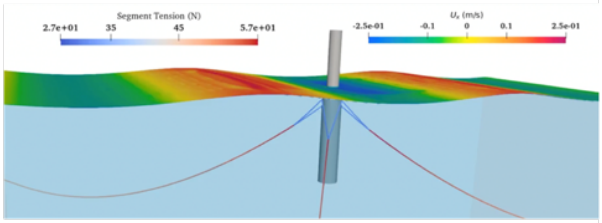

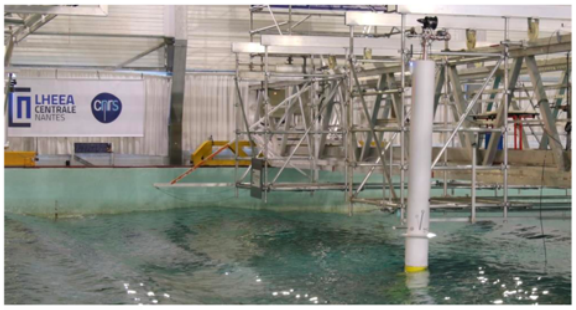

ETUDE DU SENS DE PARCOURS SUR UNE TRAJECTOIRE EN HUIT POUR UN KITE DE TRACTION AU VENT ARRIERE

STUDY OF THE DIRECTION OF MOTION OVER AN EIGHT PATTERN TRAJECTORY FOR A TRACTION KITE FULL DOWNWIND

J. BERNARD-LAMEAU[(1)], J. LOUSTAU-LAGUIDE[(1)], K. RONCIN[(1)], B. CHOUVION[(1)], L. DARIDON[(2)]

julien.bernard-lameau@ecole-air.fr ; jeremy.loustau@gmail.com ; kostia.roncin@ecole-air.fr
benjamin.chouvion@ecole-air.fr; loic.daridon@umontpellier.fr

[(1)]Centre de Recherche de l'École de l'Air, Unité de Recherche 09.401, École de l'Air et de l'Espace, 13661 Salon-de-Provence, France
[(2)]LMGC, Univ. Montpellier, CNRS, Montpellier, France

Résumé

Dans le but de réduire les émissions de gaz à effet de serre du transport maritime, la traction à l'aide de kites fait l'objet d'études ces dernières années. Dans la majorité des expérimentations, le kite réalise une trajectoire en forme de huit. Cet article étudie le sens de déplacement du kite sur cette trajectoire afin d'optimiser la force de traction. Pour cela, un modèle de dynamique du vol à trois degrés de liberté est utilisé, avec une définition simplifiée des efforts aérodynamiques. Un contrôleur basé sur un PID y est associé pour permettre le suivi de trajectoire. Les résultats montrent que la force de traction moyenne est plus importante dans le sens "down-loop". Cependant, une plus grande variation de celle-ci est observée dans le sens de déplacement optimal, ce qui peut conduire à une fatigue plus importante des câbles et de la structure du kite.

Summary

Within the frame of greenhouse gas emissions reduction from shipping, kite traction has been the subject of research in last decades. In most experiments, the kite follows a figure-of-eight trajectory. This article studies the direction of motion of the kite on this trajectory, either in 'up-loop' or in 'down-loop', in order to optimize the traction force. To this end, a three-degree-of-freedom flight dynamics model is used, with a simplified definition of the aerodynamic forces. A PID-based controller is used for trajectory tracking. The results show that the average traction force is greater in the down-loop direction. However, a greater variation is observed in the direction of optimal displacement, which can lead to greater fatigue of the cables and the kite structure.

I – Introduction

The 2023 International Maritime Organisation green house gas strategy envisages a reduction in carbon intensity of international shipping. The objective is to reduce CO2 emissions per transport work (as an average across international shipping) by at least 40% by 2030. So, in an effort to reduce carbon emissions from maritime transportation, the use of kite sails for ship propulsion has been under study since the 1980s, initially by J.F. Wellicome [13]. The development of this technology involves the study of kite trajectories, with a particular focus on optimising the traction force. However, in practice, the trajectories approximately follow a lemniscate or a horizontal eight pattern to avoid line crossings, which generate friction between them and can lead to breakage.

To investigate this problem, dynamic flight models for simulating energy production using kites were proposed by Loyd [10], these featured zero mass and point mass models. Over the past few decades, rigid body and lumped mass models have been developed employing various methods, including the Lagrangian approach introduced by Sánchez-Arriaga et al. [12], which uses rigid bars and springs to simulate the line of a rigid kite. Additionally, Eijkelhof and Schmehl [3] proposed a model employing lumped mass for the tether of a small rigid aeroplane. Lumped mass can also be used to model the deformation of the kite during simulation, as suggested by Fechner et al. [5].

Alongside the development of simulation tools, trajectory optimization has first been conducted using simple models, as proposed by Houska and Diehl [7] or by Long et al. [9]. Additionally, some optimisation work has been carried out through experimental approaches, as suggested by Fagiano and Novara [4]. However, the direction of motion along an eight pattern trajectory (if the kite goes upward or downward in the loop) has not been extensively studied. This paper addresses this gap, focusing on the subject by employing a simplified flight dynamics model based on the one proposed by Houska and Diehl [6].

The first part of this paper presents the improved model based on the one of Houska and Diehl [6] that have been developed. The key contribution of this study lies in the integration of the variation of the aerodynamic coefficient as a function of the rotation rate, allowing for the consideration of traction performance losses during turns. In the second part, the optimal direction of motion along a lemniscate is examined.

II – System modelling

This section provides a description of the mechanical model employed. Firstly, the main reference frames used are outlined. Next, the assumptions are presented and discussed, followed by a detailed presentation of the equations of mechanics and the corresponding expressions for the forces acting on the system. Subsequently, the model for controlling the kite's trajectory is explained. To conclude this section, the model is verified against existing results from Houska and Diehl [6].

Regarding the notation used in this study,vectors are indicated with an $\rightarrow$, while time derivatives are represented by dotted variables.

II – 1 Reference frames

Four reference frames are used to express the position, orientation, and aerodynamic forces acting on the kite (see figure 1) :

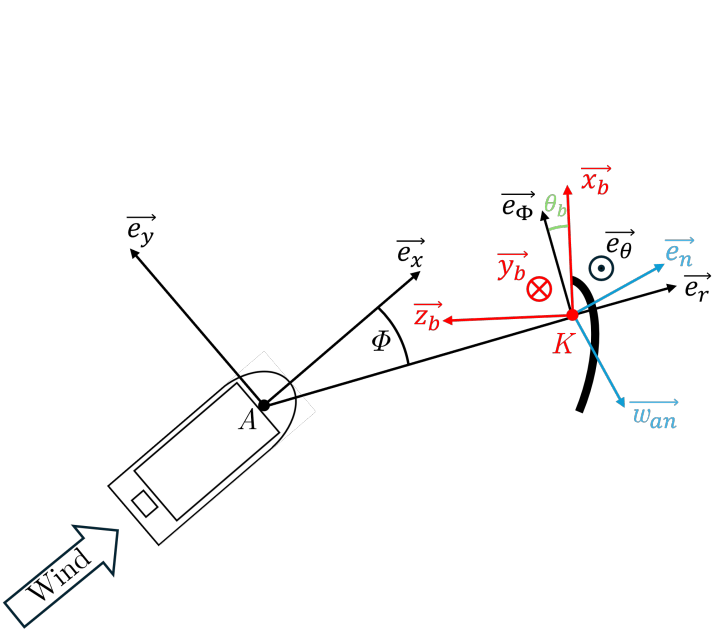

(a) Problem representation, at $\Theta = \frac{\pi}{2}$, with the boat full downwind. Consequently, the kite transverse axis $\overrightarrow{y_b}$ is equal to $\overrightarrow{e_t}$ the transverse flow reference frame vector ($\overrightarrow{y_b} = \overrightarrow{e_t}$).

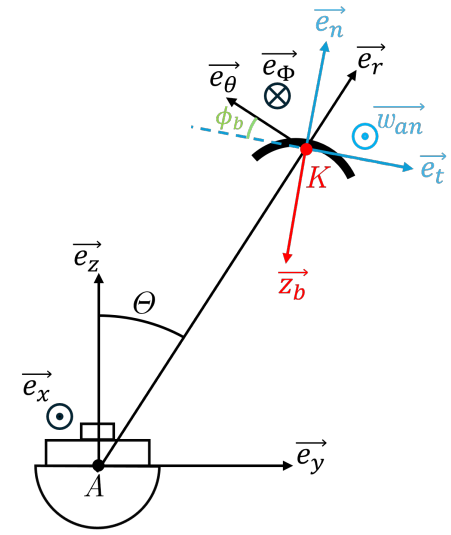

(b) Problem representation with the kite facing its apparent wind; the longitudinal kite vector $\overrightarrow{x_b}$ is equal to the azimuthal unit vector $\overrightarrow{e_\Phi}$, and unit apparent wind vector $\overrightarrow{w_{an}}$ is opposite to the longitudinal kite vector $\overrightarrow{x_b}$ ($\overrightarrow{w_{an}} = \overrightarrow{e_\Phi} = -\overrightarrow{x_b}$).

FIGURE 1 – Reference frames

— The reference frame linked to the point attached to the ship (point A), which is defined by $\overrightarrow{e_x}$, tangent to the ship trajectory (figure 1a); $\overrightarrow{e_y}$, horizontal and extends to port side of the ship (figure 1a); and $\overrightarrow{e_z}$, vertically upwards (figure 1b).

— The spherical reference frame $\{\overrightarrow{e_\Phi}, \overrightarrow{e_\Theta}, \overrightarrow{e_r}\}$. $\overrightarrow{e_r}$ is the radial unit vector which points directly outward from A to K, the center of inertia of the kite. $\overrightarrow{e_\Theta}$ is the polar unit vector which points in the direction of deacreasing co-latitude angle Θ which corresponds to motion in the vertical direction on the sphere. $\overrightarrow{e_\Phi}$ is the azimuthal unit vector defined by $\overrightarrow{e_\Phi} = \overrightarrow{e_\Theta} \wedge \overrightarrow{e_r}$.
The angles Φ and Θ, defining the kite's position in spherical coordinates are represented with uppercase letters.

— The kite's reference frame. It consists of $\overrightarrow{x_b}$, pointing from the back to the front of the kite; $\overrightarrow{y_b}$, pointing from the left wingtip to the right wingtip of the kite; and $\overrightarrow{z_b}$, pointing downwards.

— The aerodynamic frame, composed of $\overrightarrow{w_{an}}$, the unit vector collinear with the kite's apparent wind vector; $\overrightarrow{e_t}$, which lies in the plane defined by $\overrightarrow{w_{an}}$ and $\overrightarrow{y_b}$ and is orthogonal to $\overrightarrow{w_{an}}$; and $\overrightarrow{e_n}$, orthogonal to both $\overrightarrow{w_{an}}$ and $\overrightarrow{e_t}$. $\{\overrightarrow{w_{an}}, \overrightarrow{e_t}, \overrightarrow{e_n}\}$ forms a direct frame.

II – 2 Equations of motion

The method employed to derive the equations of motion is based on the point mass model developed by Houska and Diehl [6]. In this model, the kite is characterised as a point mass, allowing its orientation to be arbitrarily defined as facing it's apparent wind. It is assumed that the kite flies on a flight sphere with a constant radius, and that the lift and drag coefficients are constant. The control of the kite is achieved through the orientation

of the aerodynamic force, which is influenced by the roll angle ϕ_b. This model has been modified to incorporate lift and drag coefficients as functions of yaw rate, $\dot{\psi}_b$, as well as the moment equation in yaw. In this section, the equations governing the position are presented first, followed by the treatment of the moment equation. In the model presented here, the following equations (1)-(8) are directly extracted from the work reported in [6].

The Newton's equations are written in spherical coordinates. The unknowns are the kite's position on the flight sphere defined by the longitude Φ and colatitude Θ angles, as well as the force in the cables $\overrightarrow{F_c}$ directed along $\overrightarrow{e_r}$.

$$\frac{\overrightarrow{F_g} + \overrightarrow{F_f} + \overrightarrow{F_{aero}} - \|\overrightarrow{F_c}\|\overrightarrow{e_r}}{m_i} = \begin{pmatrix} -r\dot{\Theta}^2 - r\sin^2(\Theta)\dot{\Phi}^2 \\ r\sin(\Theta)\ddot{\Phi} + 2r\cos(\Theta)\dot{\Phi}\dot{\Theta} \\ -r\ddot{\Theta} + r\sin(\Theta)\cos(\Theta)\dot{\Phi}^2 \end{pmatrix} \tag{1}$$

Houska and Diehl introduced the notions of inertial and gravitational masses, which take into account the influence of the cables in the 2$^{\text{nd}}$ Newton's law and in the gravitational force expression [6]. The inertial mass is defined as $m_i = m_{kite} + \frac{1}{3}m_{cables}$, and the gravitational mass as $m_g = m_{kite} + \frac{1}{2}m_{cables}$. These notions are also recently re-used by Joshi et al.[8].

Gravity forces The gravity force, denoted $\overrightarrow{F_g}$, is given by eq.(2). It takes into account the Archimedes's force as well as the weight of the kite. The air density is denoted as ρ and the gravity constant g.

$$\overrightarrow{F_g} = (V\rho - m_g)\, g\overrightarrow{e_z} \tag{2}$$

Aerodynamic force on the cables The second force considered is the aerodynamic drag on cables, denoted $\overrightarrow{F_f}$. Following the model proposed by Houska and Diehl [6], it is expressed as :

$$\overrightarrow{F_f} = \frac{C_{D_C}\rho A_c}{8}\|\overrightarrow{w_a}\|\overrightarrow{w_a} \tag{3}$$

where C_{D_C} is the cable drag coefficient, A_c the projected crosswind cable area and ρ the air density.

Aerodynamic force on kite The aerodynamic force, denoted $\overrightarrow{F_{aero}}$, is decomposed into drag and lift components. These depend on the kite's yaw speed $\dot{\psi}_b$ through the aerodynamic coefficients. The force is given by :

$$\overrightarrow{F_{aero}} = \frac{1}{2}\rho C_L\left(\dot{\psi}_b\right) A_b\|\overrightarrow{w_a}\|^2\overrightarrow{e_n} + \frac{1}{2}\rho C_D\left(\dot{\psi}_b\right) A_b\|\overrightarrow{w_a}\|\overrightarrow{w_a} \tag{4}$$

A_b is the kite area, $C_L\left(\dot{\psi}_b\right)$ and $C_D\left(\dot{\psi}_b\right)$ are respectively the aerodynamic coefficients coefficient for the lift and drag components and $\overrightarrow{w_a}$ is the apparent wind speed. These quantities are defined by using the following equations proposed by Bigi et al. [2] :

$$\begin{cases} C_L\left(\dot{\psi}_b\right) = C_{L0} + k_l\sqrt{\frac{A_b}{\|\overrightarrow{w_a}\|}}|\dot{\psi}_b| \\ C_D\left(\dot{\psi}_b\right) = C_L\left(\dot{\psi}_b\right)\tan\left(GLA\left(\dot{\psi}_b\right)\right) \\ GLA\left(\dot{\psi}_b\right) = GLA_0 + k_{GLA}\sqrt{\frac{A_b}{\|\overrightarrow{w_a}\|}}|\dot{\psi}_b| \end{cases} \tag{5}$$

where the glide angle is noted GLA. GLA_0 and C_{L0} are the aerodynamic parameters of the kite without rotation speed. The coefficients k_l and k_{GLA} describe the loss of aerodynamic performance as function of the yaw velocity, for a wing of a given aspect ratio.

The apparent wind is obtained from the true wind, $\overrightarrow{w_r}$, and the kite's velocity, $\overrightarrow{v_k}$:

$$\overrightarrow{w_a} = \overrightarrow{w_r} - \overrightarrow{v_k} \tag{6}$$

in which the true wind vector is given by

$$\overrightarrow{w_r} = \left[w\left(h\right)\cos\left(\delta\right) - v_s\right]\overrightarrow{e_x} + w\left(h\right)\sin\left(\delta\right)\overrightarrow{e_y} \tag{7}$$

where δ is the angle formed between the true wind and the ship direction, $\overrightarrow{v_s}$ is the ship velocity and $w\left(h\right)$ is the wind velocity as function of the altitude, denoted h. This latter is defined with [6] :

$$w\left(h\right) = \frac{\ln\left(\frac{h}{h_r}\right)}{\ln\left(\frac{h_0}{h_r}\right)} w_0 \tag{8}$$

where w_0 is wind reference velocity at the reference altitude h_0 and h_r is a roughness length, as defined by Houska and Diehl [6] or by Maat et al. [11].

Yaw equation To simplify the model, the centre of inertia is considered to be at point K, where the aerodynamic force is applied. Additionally, the non-diagonal terms of the kite's inertia matrix are neglected, as the moment equation is solved for only one degree of rotation. This simplification helps to avoid potential discontinuities in other rotations that could yield non-physical values. This phenomenon is due to the control model, which could lead to discontinuities in the kite's roll acceleration. These assumptions lead to the equation (9) at the centre of inertia, where ψ represent the yaw angle (angles describing the kite's orientation using Euler angles are denoted with lowercase letters), $\mathcal{M}$ is the moment due to external forces, and I_{zz} denotes the moment of inertia about the yaw axis :

$$\ddot{\psi} = \frac{\mathcal{M}_{aero}}{I_{zz}} \tag{9}$$

As the gravitational force is assumed to act at the inertia centre, its moment acting on the kite at this point is zero.

The moment due to the cables is neglected because it is assumed that they are connected to freely rotating point in the vicinity of the centre of inertia.

The only moment retained in the analysis is the aerodynamic one. Around the radial axis, it depends on the kite's drift angle, and yaw rotation speed. It is given by :

$$\mathcal{M}_{aero} = \frac{1}{2}\rho\|\overrightarrow{w_a}\|^2 A_b b\left(C_{n\beta} - \frac{C_{n\dot{\beta}} b}{2\|\overrightarrow{w_a}\|}\right)\overrightarrow{e_r} \tag{10}$$

where b is the span of the kite, $C_{n\beta}$ and $C_{n\dot{\beta}}$ are the aerodynamic coefficients in yaw, linearly dependent on the drift angle and on the yaw rotation speed, such that :

$$C_{n\beta} = c_\beta \beta \qquad \text{and} \qquad C_{n\dot{\beta}} = c_{\dot{\beta}}\dot{\psi_b} \tag{11}$$

II – 3 Controller

The primary objective of the controller is to force the kite to follow a predefined trajectory, and then to be able to replicate paths observed during experiments or numerical studies. The targeted trajectory is a list of points that the kite covers until the end of the simulation. In order to control the kite trajectory, a proportional–integral–derivative controller (PID) is used.

In order to characterize the controller, two angles are defined (see figure 2a) :

— γ, the angle between $\overrightarrow{e_\Theta}$, the polar unit vector, and the kite velocity $\overrightarrow{v_k}$

— γ_{ref}, the angle between $\overrightarrow{e_\Theta}$ and the vector going from the kite position to the next targeted point, projected on the tangential plane to the flight sphere at the kite position ($\overrightarrow{e_c^p}$)

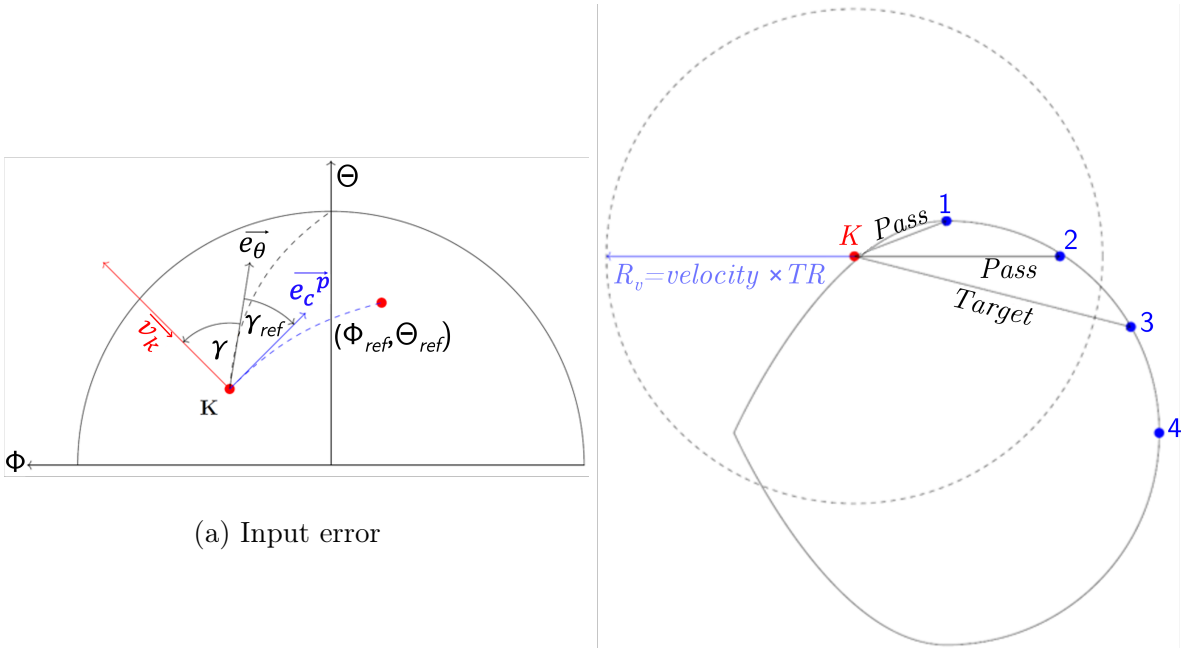

(a) Input error

(b) Points target validation

FIGURE 2 – Controller input and validation point

The input of the PID, noted ξ is defined as the difference between γ_{ref} and γ

$$\xi = \gamma_{ref} - \gamma, \tag{12}$$

while its output is the roll speed of the kite $\dot{\phi}_b$ such that :

$$\dot{\phi}_b = K_p\xi + K_i \int_0^t \xi dt + K_d\dot{\xi} \tag{13}$$

in which K_p, K_i, and K_d are respectively the proportional, integral and derivative coefficients of the controller.

To smoothen the kite's trajectory, a validation radius for the target point is employed, as illustrated in figure 2b. This feature enables the controller to target a point further ahead, facilitating better anticipation of curves and minimising abrupt changes in corrections when the controller shifts to a new target point. This validation radius, R_v, is defined by a time parameter, TR, which is multiply by the kite velocity to obtain a distance. The formula is provided in equation (14).

$$R_v = \|\overrightarrow{v_k}\| \times TR \tag{14}$$

III – Results

Before using this model, it was verified, by using assumptions and data from Houska and Diehl [6], that their results were accurately reproduced with a precision within 0.8% in terms of trajectory and traction force.

III – 1 Presentation of results

For the simulations, a kite of 5 m^2 is employed. Detailed specifications are provided in table 1. The parameters for the controller and computational settings are presented in tables 2 and 3. The simulations are done along a lemniscate trajectory defined by the equation (15) which specifies the coordinates of point i. This equation depends on the small radius R_1 and the large radius R_2, the position of the point in the target list i, and the total number of points in the targeted path denoted NB :

$$\begin{cases} \Phi_i = \frac{R_1}{2} \frac{\cos\left(\frac{2\pi i}{NB}\right)}{\sin\left(\frac{2\pi i}{NB}\right)^2+1} \\ \Theta_i = \frac{R_2}{2} \frac{\cos\left(\frac{2\pi i}{NB}\right)\sin\left(\frac{2\pi i}{NB}\right)}{0.3534\left(\sin\left(\frac{2\pi i}{NB}\right)^2+1\right)} \end{cases} \tag{15}$$

This trajectory is travelled in the both directions to be able to do a comparison between up and down-loop. Additionally, the simulations are done, first, with the targeted path centred in the flight window and, second, with an offset on the side in order to study the impact of this offset on the traction force. The same control parameters are employed for all the simulations, and provided in table 2.

To obtain reliable results, a substantial number of periods are computed, and a phase-averaging method is employed to extract the data, as done by Behrel et al [1]. Otherwise, for a single loop, discrepencies can be observed partly due to the corrections applied to follow the trajectories. Consequently, the overall evolution of the traction force over a period is less discernible.

The figure 3 and 4 show the evolution of the traction force over the period, along with the kite's trajectory. This traction is compared with the results obtained using the model proposed by Houska and Diehl [6].

For a centred path, in both directions (down-loop figure in 3a and up-loop in figure 3b), the maximums of traction are reached during the straight segments of the trajectory (between 40% and 60% of the period and 90% to 10% of the period). Conversely, the minimums of tractions occurs during the kite's turns (between 10 and 40%, and from 60% to 90% of the period). During these turns, it is possible to see that the down-loop loses more traction force compared to the up-loop. However, the down-loop exhibits a local maximum at the midpoint of its turn (at 25% of the period), which is not observed in the up-loop.

Compared to the results obtained from the model by Houska and Diehl [6], the curves exhibit similar trends. However, in figure 3a our model shows a larger traction amplitude. For the up-loop (figure 3b), the variation in traction remains comparable, though a shift to lower values is observed.

In the case of the off-centre path (figure 4), our model indicates that the maximum traction occurs during the straight segments (from 90% to 10% of the period and between 45% and 60% of the period), while the minimum is observed at the end of the more off-centre loop (at 40% of the period). Additionally, it is possible to see that the traction is slightly higher during the straight segment when the kite moves from the centre to the

TABLE 1 – Kite parameters estimated from [1]

Kite mass	2.45	kg
Cable's mass	0.5	kg
Yaw inertia	2.175	$\mathrm{kg\,m^2}$
Area	5	$\mathrm{m^2}$
Span	3	m
Volume	0.097	$\mathrm{m^3}$
C_{L0}	0.9856	-
GLA_0	0.2041	-
k_{GLA}	0.0422	s
k_l	-0.3718	$\mathrm{s\,rad^{-1}}$
c_β	0.26	-
$c_{\dot{\beta}}$	0.014	-
g	9.81	$\mathrm{m\,s^{-2}}$
Air density	1.23	$\mathrm{kg\,m^{-3}}$
Cable length	100	m
Cable drag coefficient	0.4	-
Cable diameter	0.004	m
Reference wind speed (v_0)	7	$\mathrm{m\,s^{-1}}$
h_0	40	m
h_r	0.1	m
ship velocity	0	$\mathrm{m\,s^{-1}}$
height of attached point	1	m
δ_w	0	rad

TABLE 2 – Control parameters

Limit roll speed	0.4	$\mathrm{rad\,s^{-1}}$
K_p	3	-
K_i	0.1	-
K_d	1.1	-
TR	0.4	s
Number of targeted points	500	-
R1	40	°
R2	15	°
Target centre co-latitude	70	°

TABLE 3 – Computation parameters

Time steps	0.001	s
Total simulation time	1000	s
Beginning removed part	200	s

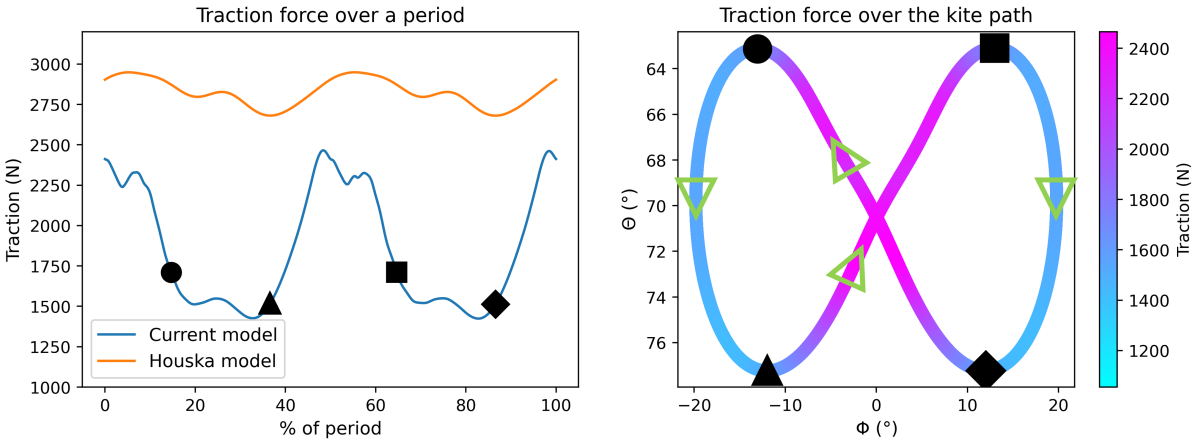

(a) Down-loop

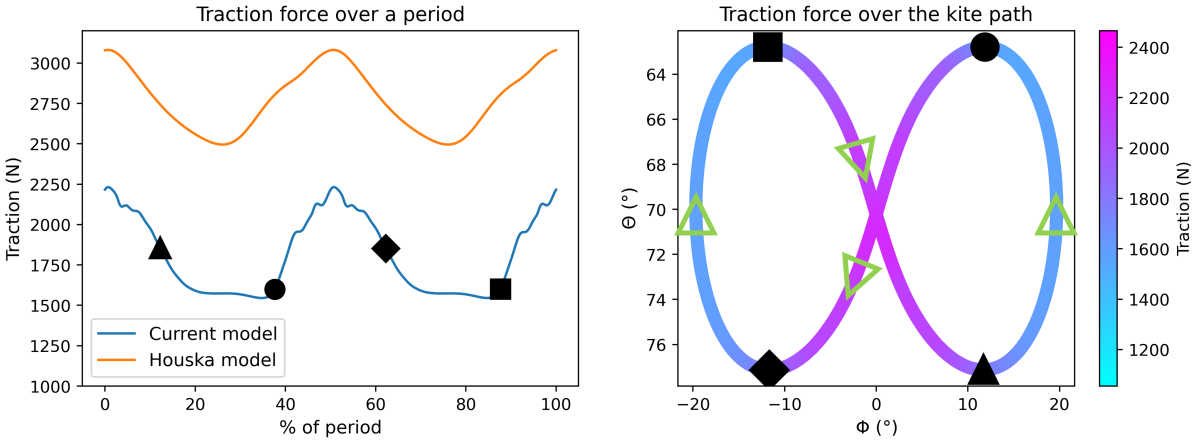

(b) Up-loop

FIGURE 3 – Traction in cable for centred paths

edge of the flight window (from 90% to 10% of the period)compared to the segment where it travels from the edge to the centre (from 45% to 65% of the period).

Compared to the model of Houska and Diehl [6], the traction follows the same trend during the first 50% of the period, which corresponds to the most off-centre segment of the trajectory. A difference is observed in the most centre half of the trajectory (between 50% and 100% of the period). In our model, there is a local minimum during the more centred loop (between 60% and 90% of the period), whereas the traction force in the Houska and Diehl model [6] continues to increase until it reaches its maximum. Furthermore, as observed in the centred path, our model shows larger variations in traction with the down-loop direction compared to the Houska and Diehl model [6], for the segment where both models show a similar trend (from 0% to 50% of the period). In contrast, for the up-loop, the variations in traction between the two models are comparable during this segment.

To be able to compare the performance over each trajectory, the maximum, minimum, mean traction force and its amplitude are given in the table 4.

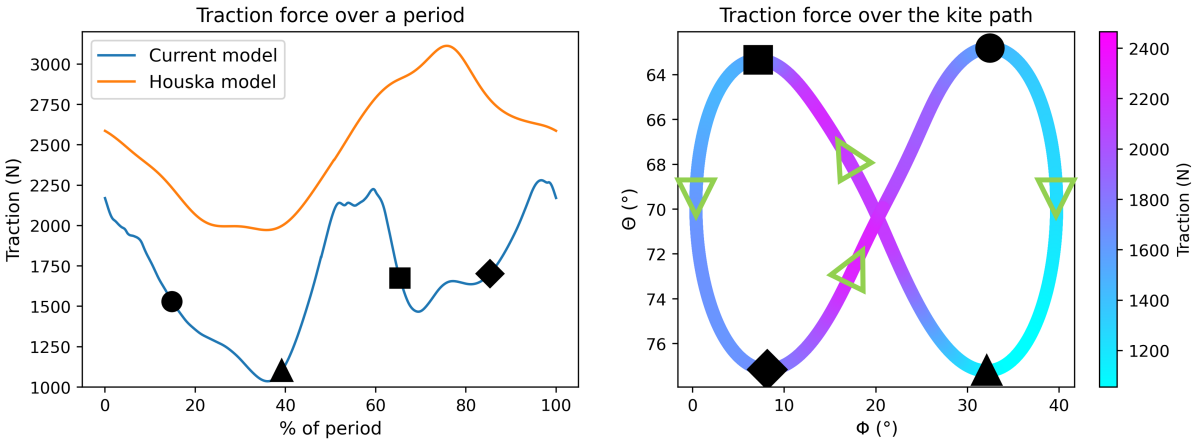

(a) Down-loop

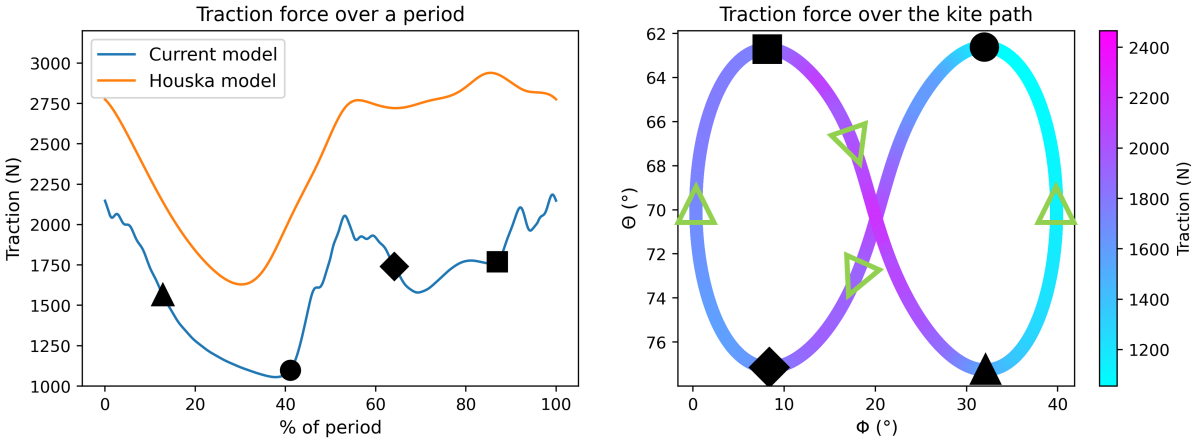

(b) Up-loop

FIGURE 4 – Traction in cable for off-centre paths

TABLE 4 – Traction study

	Mean (kN)	Loss (%)	Max (kN)	Min (kN)	Amplitude (kN)	Amplitude (%)
Centred down-loop	1.848	-	2.465	1.424	1.041	56.33
Centred up-loop	1.809	-2.110	2.232	1.545	0.687	37.98
Off-centre down-loop	1.679	-	2.280	1.036	1.244	74.09
Off-centre up-loop	1.632	-2.799	2.185	1.055	1.130	69.24

The table 4 also shows that the centred path offer 10% more traction than the off-centre path in down-loop and 11% in up-loop.

During the generation of results, it was observed that the dimensions of the target path significantly influence the controller's ability to maintain the kite on the intended trajectory. This sensitivity is partly attributed to the length of the straight segments. During these periods, the kite may oscillate around the target trajectory due to the PID controller. Depending on the "wave length" of these oscillations, relative to the length of the straight line, the kite may struggle to turn favourably at the enter of the curve. Consequently, this necessitates adjustments to the PID parameters each time the size of the figure is modified.

III – 2 Results analysis

The results presented in table 4 indicate that the down-loop trajectory generates greater traction force compared to the up-loop trajectory. However, this increased force is accompanied by a higher variation, which may contribute to greater fatigue in the cables, kite structure and winches. Additionally, as anticipated, the centred path yields more traction than the off-centre trajectory.

The additions of aerodynamic coefficients as functions of yaw rate and the yaw equation results in a lower traction force compared to the model of Houska and Diehl[6] (figure 3 and 4). This discrepancy primarily arises from the definition of the aerodynamic coefficients. As the kite rotates through a significant portion of the trajectory, its aerodynamic performance deteriorates, leading to decreased traction efficiency. This loss of performance is particularly evident on the off-centre path (figure 4) during the more centre loop. While the model by Houska and Diehl [6] predicts a maximum traction force, our model indicates a local minimum instead.

The simulations conducted in both directions for a lemniscate trajectory illustrate the impact of gravity on control. It is observed that for both centred and off-centre paths, the down-loop shows a greater traction amplitude than the up-loop, which contrasts with the findings of Houska and Diehl [6]. Additionally, during turns, the traction force is greater for the up-loop than for the down-loop along the centred path. These observations are not consistent with the expectation that gravity would assist the kite in increasing its velocity during turns, thereby generating a larger traction force. This discrepancy may come from the controller requiring larger corrective actions to maintain the trajectory in the down-loop, in order to counteract the gravitational force at the end of the turns.

On our result for off-centre path (figure 4) it is possible to see that the kite generates more traction force when moving from the centre to the edge of the flight window compared to the reverse direction. This occurs because the real wind and the wind induced by the kite's velocity are more aligned in this direction. In contrast, during the other straight segment, these two wind components are partially opposed. As a result, the apparent wind is significantly stronger in one direction, which affects the aerodynamic force, so the resulting traction force.

IV – Discussion

The results presented here are derived from a simplified model of the kite that accounts for only three of the six degrees of freedom applicable to a rigid body. Furthermore, the model does not incorporate structural deformation. A simplified representation is adopted that considers only the influence of yaw rate on the lift and drag coefficients (eq.(5)). For the aerodynamic moment, only the drift angle and the yaw rate are taking into account (eq.(10)). Consequently, these limitations mean that not all aspects of the wing's aerodynamic behaviour are accurately represented, such as variations in angle of attack for example. Further studies taking into account influences from other parameters could improve the model reliability.

As the straight segments offer a maximums of traction and the minimums occur during turns, the ratio between the size of the loops and the size of the straight segment could be investigate to obtained the optimal size for an eight figure. Additionally, the controller should aim to minimise corrections to prevent a decrease in aerodynamic performance.

V – Conclusion

Using a simplified 3 degrees of freedom model that takes into account the kite yaw equation, it has been determined that the down-loop trajectory generates a greater traction force compared to the up-loop trajectory. However, this gain is accompanied by a greater variability in traction force, which may contribute to increase fatigue in the cables and structure. This study also highlights the importance of having an effective controller that can follow the trajectory without requiring manual adjustments in response to changes in the problem parameters. Furthermore, to optimise traction force, it is essential for the controller to minimise corrections, thereby improving overall traction performance.

Références

[1] M. Behrel, K. Roncin, J.-B. Leroux, F. Montel, R. Hascoet, A. Neme, C. Jochum, and Y. Parlier. Application of phase averaging method for measuring kites performance : Onshore results. *Journal of Sailing Technology*, 3(01) :1–29, Sept. 2018.

[2] N. Bigi, K. Roncin, J.-B. Leroux, and Y. Parlier. Ship towed by kite : Investigation of the dynamic coupling. *Journal of Marine Science and Engineering*, 8(7) :486, July 2020.

[3] D. Eijkelhof and R. Schmehl. Six-degrees-of-freedom simulation model for future multi-megawatt airborne wind energy systems. *Renewable Energy*, 196 :137–150, Aug. 2022.

[4] L. Fagiano and C. Novara. Automatic crosswind flight of tethered wings for airborne wind energy : a direct data-driven approach. *IFAC Proceedings Volumes*, 47(3) :4927–4932, 2014.

[5] U. Fechner, R. van der Vlugt, E. Schreuder, and R. Schmehl. Dynamic model of a pumping kite power system. *Renewable Energy*, 83 :705–716, Nov. 2015.

[6] B. Houska and M. Diehl. Optimal control of towing kites. In *Proceedings of the 45th IEEE Conference on Decision and Control*, volume 613, pages 2693–2697. IEEE, 2006.

[7] B. Houska and M. Diehl. Optimal control for power generating kites. In *2007 European Control Conference (ECC)*. IEEE, July 2007.

[8] R. Joshi, R. Schmehl, and M. Kruijff. Performance modelling and scaling of fixed-wing ground-generation airborne wind energy systems. *Wind Energy Science*, Aug. 2024.

[9] X. Long, M. Sun, M. Piao, and Z. Chen. Parameterized trajectory optimization and tracking control of high altitude parafoil generation. *Energies*, 14(22) :7460, Nov. 2021.

[10] M. L. Loyd. Crosswind kite power (for large-scale wind power production). *Journal of Energy*, 4(3) :106–111, May 1980.

[11] N. Maat, C. Kraan, and W. Oost. The roughness of wind waves. *Boundary-Layer Meteorology*, 54 :89–103, 1991.

[12] G. Sánchez-Arriaga, A. Pastor-Rodríguez, M. Sanjurjo-Rivo, and R. Schmehl. A lagrangian flight simulator for airborne wind energy systems. *Applied Mathematical Modelling*, 69 :665–684, May 2019.

[13] J. Wellicome. Some comments on the relative merits of various wind propulsion devices. *Journal of Wind Engineering and Industrial Aerodynamics*, 20(1–3) :111–142, July 1985.